A&A 626, L3 (2019)
https://doi.org/10.1051/0004-6361/201935577

Astronomy & Astrophysics

LETTER TO THE EDITOR

The Close AGN Reference Survey (CARS)

Discovery of a global [C II] 158 μm line excess in AGN HE 1353−1917

I. Smirnova-Pinchukova[1], B. Husemann[1], G. Busch[2], P. Appleton[3], M. Bethermin[4], F. Combes[5], S. Croom[6], T. A. Davis[7], C. Fischer[8], M. Gaspari[9,⋆], B. Groves[10], R. Klein[11], C. P. O'Dea[12,13], M. Pérez-Torres[14,15], J. Scharwächter[16], M. Singha[12], G. R. Tremblay[17], and T. Urrutia[18]

[1] Max-Planck-Institut für Astronomie, Königstuhl 17, 69117 Heidelberg, Germany
e-mail: smirnova@mpia.de
[2] I. Physikalisches Institut der Universität zu Köln, Züplicher Str. 77, 50937 Köln, Germany
[3] Caltech/IPAC, 1200 E. California Blvd., Pasadena, CA 91125, USA
[4] Aix Marseille Univ., CNRS, CNES, LAM, Marseille, France
[5] LERMA, Observatoire de Paris, PSL Research Univ., Collège de France, CNRS, Sorbonne Univ., UPMC, Paris, France
[6] Sydney Institute for Astronomy, School of Physics, A28, The University of Sydney, NSW 2006, Australia
[7] School of Physics & Astronomy, Cardiff University, Queens Buildings, The Parade, Cardiff CF24 3AA, UK
[8] Deutsches SOFIA Institut, Pfaffenwaldring 29, 70569 Stuttgart, Germany
[9] Department of Astrophysical Sciences, Princeton University, 4 Ivy Lane, Princeton, NJ 08544-1001, USA
[10] Research School of Astronomy and Astrophysics, The Australian National University, Cotter Road, Weston, ACT 2611, Australia
[11] SOFIA-USRA, NASA Ames Research Center, MS 232-12, Moffett Field, CA 94035, USA
[12] Department of Physics & Astronomy, University of Manitoba, Winnipeg, MB R3T 2N2, Canada
[13] School of Physics & Astronomy, Rochester Institute of Technology, 84 Lomb Memorial Drive, Rochester, NY 14623, USA
[14] Instituto de Astrofísica de Andalucía, Glorieta de las Astronomía s/n, 18008 Granada, Spain
[15] Departamento de Física Teórica, Facultad de Ciencias, Universidad de Zaragoza, 50009 Zaragoza, Spain
[16] Gemini Observatory, Northern Operations Center, 670 N. A'ohoku Pl., Hilo, Hawaii 96720, USA
[17] Center for Astrophysics, Harvard & Smithsonian, 60 Garden St., Cambridge, MA 02138, USA
[18] Leibniz-Institut für Astrophysik Potsdam, An der Sternwarte 16, 14482 Potsdam, Germany

Received 29 March 2019 / Accepted 29 April 2019

ABSTRACT

The [C II]λ158 μm line is one of the strongest far-infrared (FIR) lines and an important coolant in the interstellar medium of galaxies that is accessible out to high redshifts. The excitation of [C II] is complex and can best be studied in detail at low redshifts. Here we report the discovery of the highest global [C II] excess with respect to the FIR luminosity in the nearby AGN host galaxy HE 1353−1917. This galaxy is exceptional among a sample of five targets because the AGN ionization cone and radio jet directly intercept the cold galactic disk. As a consequence, a massive multiphase gas outflow on kiloparsec scales is embedded in an extended narrow-line region. Because HE 1353−1917 is distinguished by these special properties from our four bright AGN, we propose that a global [C II] excess in AGN host galaxies could be a direct signature of a multiphase AGN-driven outflow with a high mass-loading factor.

Key words. galaxies: Seyfert – galaxies: star formation – ISM: jets and outflows – infrared: ISM

1. Introduction

The [C II] 157.74 μm emission line arises from the fine-structure transition $^2P_{3/2} \rightarrow {}^2P_{1/2}$ of the ground state of singly ionized carbon C^+ (ionization potential of 11.2 eV). Working as a coolant in multiple phases of the interstellar medium (ISM), the [C II] line is one of the brightest emission lines in the far-infrared (FIR); it contributes 0.1–0.3% to the FIR luminosity.

The [C II] line has been calibrated as a probe for the cold gas content and associated star formation rates (SFR) in galaxies (Stacey et al. 1991; Boselli et al. 2002; Herrera-Camus et al. 2015). However, using the [C II] line as an SFR tracer is complex because of the multiple mixed excitation mechanisms of the line. In local star-forming galaxies, 66–82 % of [C II] arises from the neutral gas of photodissociation regions (PDRs), and the rest comes from the ionized phase (Croxall et al. 2017). The mechanism of dust infrared emission, on the other hand, is rather simple: dust preferentially absorbs UV radiation from the stellar population and therefore is sensitive to the bright young stars. The infrared luminosity has been well calibrated as an SFR tracer at SFR $>1\,M_\odot\,\mathrm{yr}^{-1}$ (Hirashita et al. 2003; Murphy et al. 2011) so that the [C II] and FIR luminosity are expected to be correlated.

At the highest SFRs, luminous and ultra-luminous infrared galaxies (U/LIRGs) exhibit the so-called [C II] line deficit (Helou et al. 2001; Malhotra et al. 2001; Luhman et al. 2003), where [C II] becomes unreliable as an SFR indicator (Díaz-Santos et al. 2013). The origin of the line deficit is still debated and is directly connected to physical processes that are crucial for understanding the [C II] excitation mechanisms.

⋆ Lyman Spitzer Jr. fellow.

Table 1. Measured galaxy properties.

Object	D_L [Mpc]	$F_{[C\,II]}$ 10^{-13} [erg s cm^{-2}]	F_{FIR} (*) 10^{-11} [erg s cm^{-2}]
HE 0433−1028	156.4	6.13 ± 0.45	9.41 ± 0.05
HE 1029−1831	177.7	5.32 ± 0.83	9.82 ± 0.33
HE 1108−2813	104.7	2.65 ± 0.24	11.86 ± 0.32
HE 1353−1917	154.0	5.07 ± 0.32	1.11 ± 0.04
HE 2211−3903	175.2	1.17 ± 0.41	1.94 ± 0.25

Notes. (*)Integrated over 42.5–122.5 μm.

Active galactic nuclei (AGN) are able to affect the [C II]/FIR ratio in several ways: they can increase the infrared luminosity through dust heating (Herrera-Camus et al. 2018a); act as an additional source of the [C II] excitation; or suppresses the [C II] line through the overionization of C^+ to $C^{2+,3+,etc.}$ with their hard radiation field (Langer & Pineda 2015). *Herschel* surveys of nearby galaxies such as KINGFISH (Smith et al. 2017) and SHINING (Herrera-Camus et al. 2018b) found no link between the [C II] line emission and AGN luminosity, but these AGN may be not luminous enough to outshine the star formation.

Given its brightness, the [C II] line is the most important ISM diagnostic at high redshifts that can be observed with unprecedented spatial resolution and depth on submillimeter interferometers. The sample of the observed high-redshift objects includes starburst and AGN-dominated systems, with the [C II]/FIR ratios spanning a wide range from 0.02% to 5% (e.g., Gullberg et al. 2015; Brisbin et al. 2015; Decarli et al. 2018). In order to provide an interpretation, we need to investigate the [C II] emission in local galaxies and determine the effect of luminous AGN.

In this Letter, we present [C II] line observations with the Stratospheric Observatory For Infrared Astronomy (SOFIA, Temi et al. 2014) for five nearby ($0.024 < z < 0.040$) luminous Seyfert 1 AGN host galaxies from the Close AGN Reference Survey (CARS; Husemann et al. 2017)[1] to investigate the impact of AGN on the global [C II] luminosity.

Throughout the paper, we assume a flat cosmological model with $H_0 = 70\,\mathrm{km\,s^{-1}\,Mpc^{-1}}$, $\Omega_M = 0.3$, and $\Omega_\Lambda = 0.7$.

2. Observations and analysis

2.1. SOFIA/FIFI-LS observations

We observed five CARS objects with the Far Infrared Field-Imaging Line Spectrometer (FIFI-LS; Klein et al. 2014) on board SOFIA. The objects were picked to cover a broad range of SFRs (1–11 $M_\odot\,\mathrm{yr^{-1}}$) and avoid the strong atmospheric absorption in the redshifted [C II] line wavelength region. The SFR estimates were initially based on the predictions calculated from the AGN-subtracted extinction-corrected Hα line from observations obtained with the Mulit-Unit Spectroscopic Explorer (MUSE; Bacon et al. 2010, Sect. 2.2). The properties of the observed galaxies are listed in Table 1.

The observations were performed during SOFIA Cycle 4 (plan ID 04_0056, PI: Husemann) and Cycle 5 (plan ID 05_0077, PI: Husemann). FIFI-LS is a double-beam spectrometer that covers $1' \times 1'$ in the red channel (105–200 μm) and $0.5' \times 0.5'$ in the blue channel (50–125 μm), split up into 5×5 spatial pixels. We tuned the setups to cover the [C II] line in the red channel with spectral resolution of $R \sim 1200$ (250 km s^{-1}) and either [O III] 88 μm or [O I] 63 μm in the blue channel, depending on atmospheric transmission.

The pipeline-processed data are provided by the FIFI-LS team. We used LEVEL_3 science-ready data, which consist of a number of ∼30 s exposures, to apply an additional selection (see Appendix A for details) and background subtraction, and constructed data cubes with 6″ sampling using the Drizzle algorithm (Fruchter et al. 1997). To derive total [C II] line fluxes from the FIFI-LS cubes, we summed the spectra within an aperture with 36″ diameter and fit the line shape with Gaussian profiles. The HE 1108−2813 and HE 2211−3903 spectra are well modeled by a single-Gaussian component, while the spectra of HE 0433−1028, HE 1029−1831 and HE 1353−1917 require two Gaussian components. The spectra and the fitting results together with the excluded wavelength ranges due to the strong atmospheric absorption regions[2] are shown in Fig. 1. In addition, we have analyzed the blue channel FIFI-LS data for HE 1353−1917 to estimate the upper limit of the [O III] 88 μm emission line flux $<4.8\times10^{-13}$. The [C II] best-fit shape was used in the [O III] upper limit estimation, taking into account the spectral resolution of $R \sim 670$ (450 km s^{-1}) for the observed wavelengths.

2.2. VLT/MUSE observations

All five CARS targets were observed with MUSE at the Very Large Telescope (VLT) under ESO programs 094.B-0345(A) and 095.B-0015(A). The MUSE data cover $1' \times 1'$ FoV at a 0.″2 spatial sampling and a wavelength coverage of 4650–9300 Å with $R \sim 2500$. Integration times range from 400 s–900 s split up into two or three exposures, which are rotated by 90° against each other for cosmic-ray rejection and better image cosmetics. The data were reduced with the standard MUSE pipeline (version 1.6.0, Weilbacher et al. 2012, 2014).

As a first step in the post-processing, we subtracted the bright point-like AGN emission from the reconstructed datacube using QDeblend^{3D}, as described in Husemann et al. (2013, 2014, 2019). Afterward we modeled the stellar continuum and ISM emission lines in the AGN-subtracted datacube with PyParadise (see Husemann et al. 2016; Weaver et al. 2018, for details).

In Fig. 2 we show the classical Baldwin-Philips-Terlevich (BPT; Baldwin et al. 1981) diagrams and corresponding spatial maps for the targeted galaxies after binning 8×8 pixels. Essentially, the BPT diagnostic diagrams highlight different dominating ionization mechanisms. The face-on galaxies display line ratios that are mainly consistent with star formation or intermediate line ratios between star formation and AGN excitation. The edge-on galaxy HE 1353−1917 is instead dominated by AGN photoionization. The fraction of AGN excitation to the extinction-corrected Hα for HE 1353−1917 is >80%, whereas a fraction of <40% is found for all face-on galaxies.

2.3. SED fitting and FIR luminosities

We constructed spectral energy distributions (SEDs) for all targets using publicly available broad-band photometry from the following catalogs: the *Herschel*/SPIRE Point Source Catalogue (Schulz et al. 2017), the AKARI/FIS Bright Source Catalogue (Yamamura et al. 2009), the 2MASS Extended Source Catalog (Jarrett et al. 2000), and the GALEX Source Catalog (Bianchi et al. 2017). For the following datasets we applied aperture measurements on the survey images: *Herschel*/PACS images from

[1] www.cars-survey.org

[2] Based on the ATRAN tool by Steve Lord, https://atran.arc.nasa.gov/cgi-bin/atran/atran.cgi

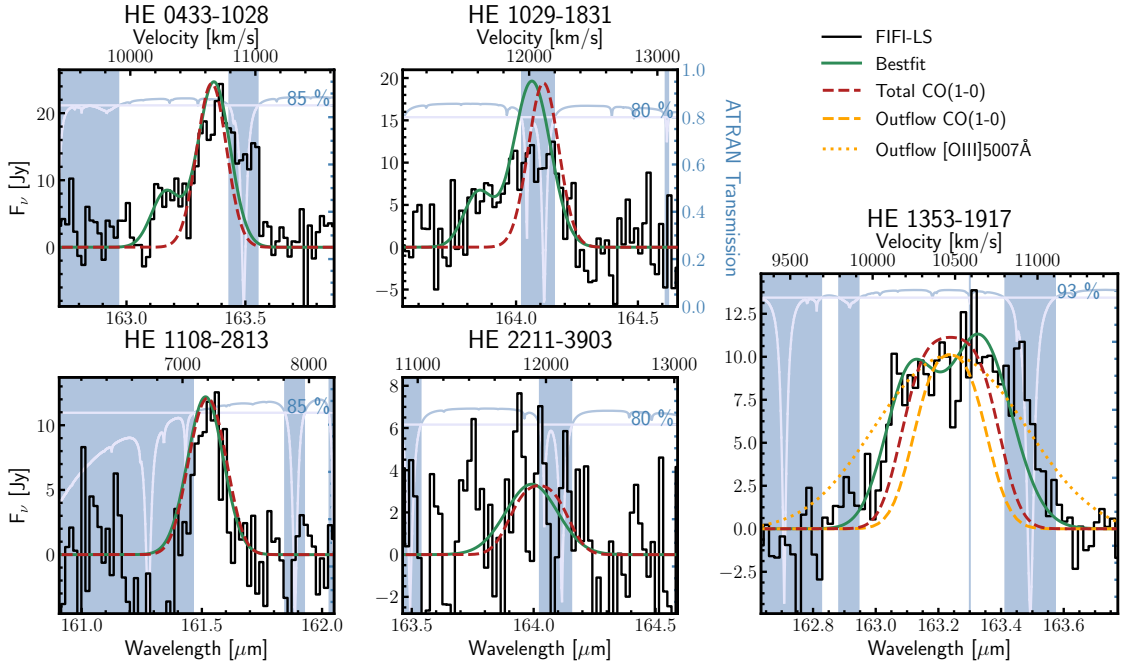

Fig. 1. SOFIA/FIFI-LS [C II] spectra (black lines) for each object integrated within 36″ diameter apertures. The CO(1–0) and best-fit Gaussian or double-Gaussian profiles are shown as red dashed and solid green lines, respectively. The CO(1–0) and [O III]5007 Å line profiles of the HE 1353−1917 outflow are shown as orange dashed and dotted lines. The comparison line profiles are degraded to the spectral resolution of SOFIA. The atmospheric transmission curves are shown in blue, and the shaded regions of low transmission are excluded from the analysis.

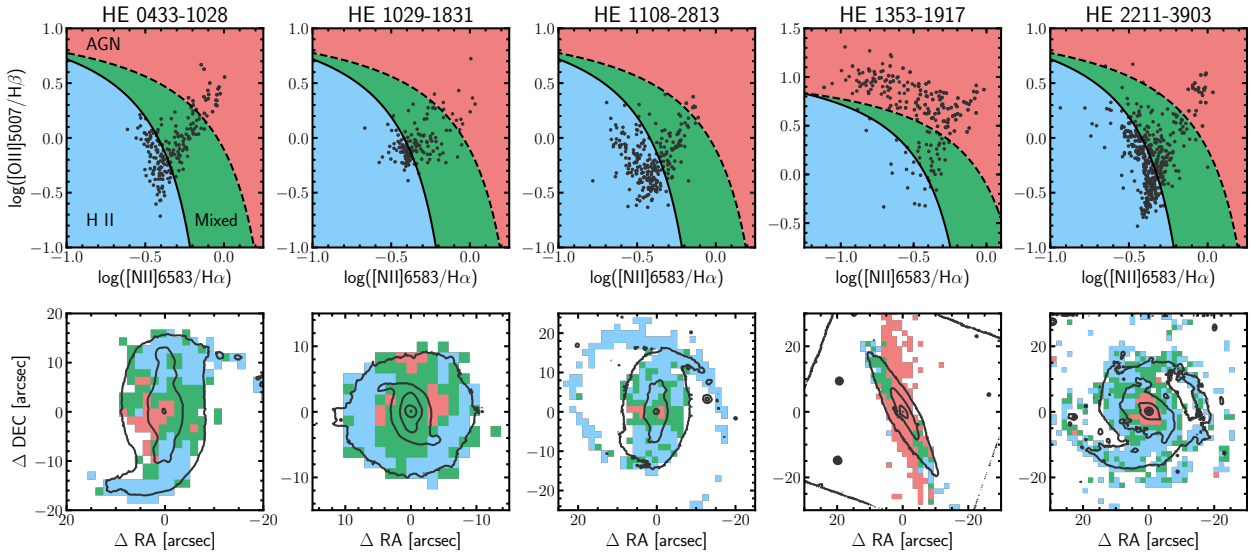

Fig. 2. *Upper panel*: MUSE BPT diagnostic diagrams with empirical dividing lines. The solid line shows data from Kauffmann et al. (2003) and the dashed line from Kewley et al. (2001). The colors represent AGN ionization (red), ionization by H II regions (blue), and mixed regime (green). *Lower panel*: MUSE emission line 1.6″ × 1.6″ binned maps color-coded according to the BPT diagram regions; white-light contours are overplotted in black.

the *Herschel* Science Archive[3], WISE Image Atlas (Cutri et al. 2011), optical *grizy* photometric images[4] from the Pan-STARRS DR1 (Chambers et al. 2016), and *Swift*/UVOT images from the Barbara A. Mikulski Archive for Space Telescopes[5].

We obtained the FIR (42.5–122.5 μm) luminosities through SED fitting with AGNfitter (Calistro Rivera et al. 2016). AGNfitter uses an MCMC approach and various template libraries to model the SED as a super-position of emission from an AGN accretion disk, a torus of AGN-heated dust, stellar light from the galaxies, and cold dust in star-forming regions. The AGNfitter output SED models are shown in Appendix B and the FIR (42.5–122.5 μm) luminosities are listed in the Table 1.

3. Results and discussion

The [C II] and FIR luminosities of our five targets are shown in Fig. 3 in comparison to a large literature compilation of low-redshift galaxies from Herrera-Camus et al. (2018a). Four of the CARS targets lie within the 3σ region of the mean relation, while

[3] HSA, http://archives.esac.esa.int/hsa/whsa/
[4] http://ps1images.stsci.edu
[5] MAST; http://archive.stsci.edu/

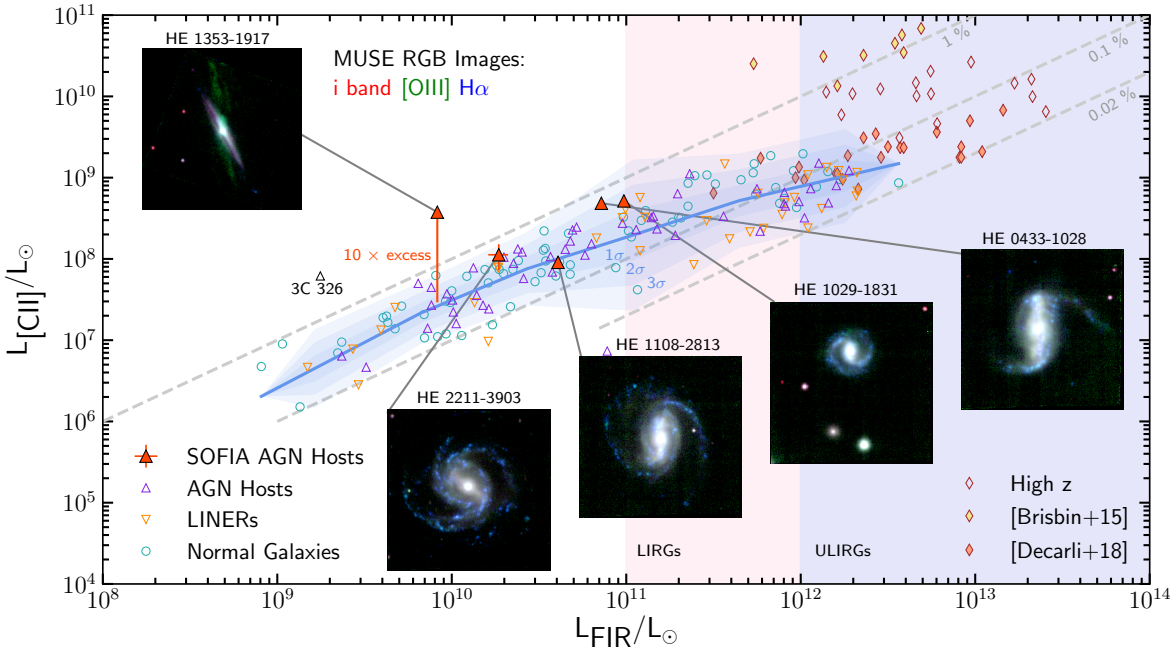

Fig. 3. [C II] line luminosity as a function of FIR luminosity. Our five CARS targets are shown as red triangles compared to the literature compilation of Herrera-Camus et al. (2018a): normal star-forming and star-burst galaxies (green circles), AGN host galaxies (purple triangles), LINER galaxies (orange upside-down triangles), and high-redshift galaxies including the samples from Brisbin et al. (2015) and Decarli et al. (2018) (brown diamonds). The blue line is the mean of the low-redshift galaxies distribution, and the blue-shaded areas correspond to 1, 2, and 3σ. Pink and purple shades represent LIRG $L_{\rm FIR} > 10^{11}$ and ULIRG $L_{\rm FIR} > 10^{12}$ regimes. The luminosities for 3C 326 are taken from Guillard et al. (2015).

HE 1353−1917 lies above the relation with more than 7σ significance. The outlier has the strongest deviation from the mean trend observed so far at low redshift, with an unprecedented global [C II] line excess of an order of magnitude. AGN hosts and LINERs tend to be below the relation in the (U)LIRG regime $L_{\rm FIR} > 10^{11}\,L_{\odot}$ and more likely show [C II] line deficits.

Based on the FIR and AGN-subtracted extinction-corrected Hα luminosity, we expected HE 1353−1917 to be the faintest target in [C II], but it turned out to be the brightest source of our sample. While all galaxies have similar metallicities, stellar masses, and AGN bolometric luminosities, the obvious dissimilarity is the edge-on orientation of HE 1353−1917. When we consider the unobscured nature of this AGN, this means that the AGN ionization cone directly pierces the gas-rich disk of the galaxy. This leads to a large biconical extended narrow-line region (ENLR) that is oriented almost along the disk axis on kiloparsec scales, as clearly shown in Fig. 2. In addition, a massive multiphase outflow on kiloparsec scales with a mass outflow rate of $\dot{M}_{\rm out}$ ~10–100 $M_{\odot}\,{\rm yr}^{-1}$ is detected in this galaxy, as discussed in detail by Husemann et al. (2019), while less prominent outflows are detected in the other four galaxies (Singha et al., in prep.). The global SFR of ~2 $M_{\odot}\,{\rm yr}^{-1}$ implies an integrated mass-loading factor of ~10 or more that has a similar scale as the observed [C II] excess.

Several powering sources may contribute to the [C II] line excess in HE 1353−1917, but the challenge is to distinguish the dominant [C II] line excitation mechanism. As highlighted in Fig. 3, the [C II] line luminosity of HE 1353−1917 cannot be powered by the star formation alone. The SFRs calculated from the extinction-corrected Hα ($\rm SFR_{H\alpha} = 1.23 \pm 0.03\,M_{\odot}yr^{-1}$) and 42.5–122.5 μm luminosity ($\rm SFR_{FIR} = 2.3 \pm 0.1\,M_{\odot}yr^{-1}$) can account for only about 25% of the observed [C II] line luminosity ($\rm SFR_{[C\,II]} = 2.286 \times 10^{-43} \times L_{[C\,II]}^{1.034}$, Herrera-Camus et al. 2015). X-ray dominated regions (XDRs) produced by the hard X-ray photons from an AGN may contribute and even dominate the PDR [C II] emission. From the scaling relation $L_{\rm [C\,II],XDR} = 2 \times 10^{-3}\,L_{\rm 2-10\,keV}$ by Stacey et al. (2010), we estimate an XDR contribution of only 10% given an X-ray luminosity of $L_{\rm 2-10\,keV} = 1.69 \times 10^{43}\,{\rm erg\,s^{-1}}$ (Husemann et al. 2019).

[C II] emission can originate in any gas phase that is illuminated by UV photons. Using other line and continuum diagnostics, we can obtain some idea of which phases contribute to the [C II] emission, for example, 66–82% for the neutral phase and the rest for the ionized phase in local star-forming galaxies (Croxall et al. 2017). However, these fractions do not necessarily remain the same in the ENLR of an AGN. How much of the [C II] emission originates from an ENLR has not been systematically explored so far. If the ionized gas phase produces more than 20–40% of [C II] as in PDR paradigm, then it can explain the observed [C II] excess. In HE 1353−1917 only ~20% of Hα originates from star-forming regions and ~80% comes from the AGN-ionized regions. If we naively assume that 20% of the [C II] flux originates from star formation, the $\rm [C\,II]_{SF}$ of HE 1353−1917 falls within 3σ of the [C II]–FIR relation.

Dissipation of the kinetic energy of shocks and outflows can also have important consequences on the [C II] emission, as theoretically explored by Lesaffre et al. (2013). [C II]/FIR ratios of 3–7% are detected in between merging galaxies (Appleton et al. 2013; Peterson et al. 2018) and locally within galaxies (Appleton et al. 2018). On the global scale, the radio galaxy 3C 326 emits around 3% of FIR in [C II] line for which jet-driven turbulence is likely responsible (Guillard et al. 2015). Nesvadba et al. (2010) estimated an outflow rate in 3C 326 of $\dot{M}_{\rm out} \sim 35\,M_{\odot}\,{\rm yr}^{-1}$, compared to the SFR ~ 0.1 $M_{\odot}\,{\rm yr}^{-1}$ (Ogle et al. 2007), brings a mass-loading factor of >10 similar to that found in HE 1353−1917. HE 1353−1917 has a global [C II]/FIR ratio of 4.3 ± 0.4% and a radio-jet powering the multiphase gas outflow (Husemann et al. 2019). The [C II] line width of $760 \pm 60\,{\rm km\,s^{-1}}$ is broader than the CO(1-0) line for cold molecular gas outflow ~210 $\rm km\,s^{-1}$, but narrower than the ionized gas outflow ~1020 $\rm km\,s^{-1}$ (see Fig. 1). [C II]

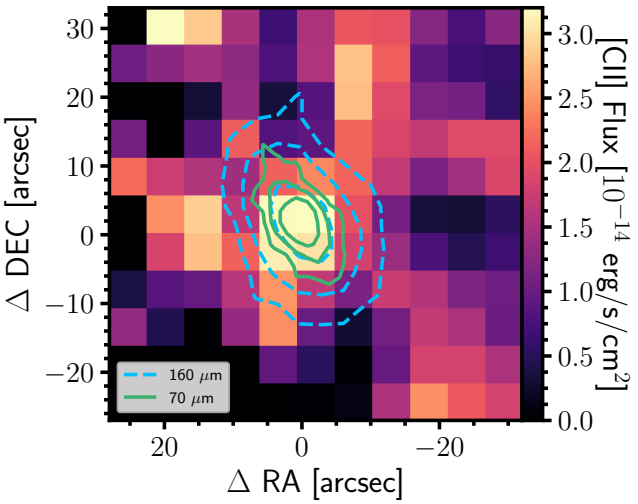

Fig. 4. SOFIA/FIFI-LS [C II] line flux map of HE 1353 − 1917. The contours represent *Herschel* PACS 70 (solid green lines) and 160 μm (blue dashed line) photometric observations.

therefore likely traces the interface between the warm and cold gas phase within the outflow. We can relate the region where the [C II] excess occurs to the center of the galaxy (Fig. 4) where the brightest region of the ENLR and the kpc-scale multi-phase outflow are indeed located. The [O III] upper limit implies a line ratio limit of [O III]/[C II] <0.96, which suggests that the pure AGN ionization in the ENLR is not the primary cause for the [C II] excess. Hence, the observations are firm evidence that the [C II] line excess in HE 1353−1917 is related to the multiphase outflow initiated by the jet.

High-redshift galaxies span an entire range between [C II] deficient and normal regimes with [C II]/FIR ratios from 0.02% to 5%. The large scatter in the ratios may be caused by the order-of-magnitude difference in spatial resolutions, for instance, 18″ for CSO, Brisbin et al. (2015) with average ratio of 1.8% and 1″ for ALMA, Decarli et al. (2018) with average ratio of 0.08%, as low-resolution observations can include a larger fraction of intergalactic [C II] emission. Several high-redshift QSO have shown a [C II] enhancement (Maiolino et al. 2009; Wagg et al. 2010), which was interpreted as due to a low metallicity given the high [C II]/FIR and [C II]/CO(1 − 0) ratios in local dwarf galaxies. We measured [C II]/FIR ∼ 4% and [C II]/CO(1−0) ∼ 10^4 for HE 1353−1917, which can neither be explained by intergalactic [C II] emission nor by a low metallicity.

4. Conclusion

We presented the discovery of a global [C II] line excess in one out of five AGN host galaxies. Based on ancillary information from an extensive multiwavelength analysis of this galaxy as part of the CARS survey, we can directly connect the [C II] line excess in HE 1353−1917 to the impact of the AGN that drives a massive multiphase outflow on kiloparsec scales embedded in an ENLR (Husemann et al. 2019). The detection of such a global [C II] excess in AGN host galaxies is of crucial importance for the interpretation of [C II] line observations and the detection of massive gas outflows in luminous high-redshift AGN host galaxies. Given the evidence of HE 1353−1917 and the similar outflow seen in 3C 326, we propose that a significant [C II] line excess in luminous AGN, if detected, can be used as an inference for a multiphase AGN outflow with a high mass-loading factor even at high redshifts.

Acknowledgements. We thank the anonymous referee for helpful comments that improved the quality of the manuscript. Based on observations made with the NASA/DLR Stratospheric Observatory for Infrared Astronomy (SOFIA). SOFIA is jointly operated by the Universities Space Research Association, Inc. (USRA), under NASA contract NNA17BF53C, and the Deutsches SOFIA Institut (DSI) under DLR contract 50 OK 0901 to the University of Stuttgart. Based on observations collected at the European Organization for Astronomical Research in the Southern Hemisphere under ESO programme 094.B-0345(A) and 095.B-0015(A). M.G. is supported by the Lyman Spitzer Jr. Fellowship (Princeton University) and by NASA Chandra GO7-18121X and GO8-19104X. M.P.T. acknowledges support from the Spanish MINECO through grant AYA2015-63939-C2-1-P.

References

Appleton, P. N., Guillard, P., Boulanger, F., et al. 2013, ApJ, 777, 66
Appleton, P. N., Diaz-Santos, T., Fadda, D., et al. 2018, ApJ, 869, 61
Bacon, R., Accardo, M., Adjali, L., et al. 2010, in Ground-based and Airborne Instrumentation for Astronomy III, Proc. SPIE, 7735, 773508
Baldwin, J. A., Phillips, M. M., & Terlevich, R. 1981, PASP, 93, 5
Bianchi, L., Shiao, B., & Thilker, D. 2017, ApJS, 230, 24
Boselli, A., Gavazzi, G., Lequeux, J., & Pierini, D. 2002, A&A, 385, 454
Brisbin, D., Ferkinhoff, C., Nikola, T., et al. 2015, ApJ, 799, 13
Calistro Rivera, G., Lusso, E., Hennawi, J. F., & Hogg, D. W. 2016, ApJ, 833, 98
Chambers, K. C., Magnier, E. A., Metcalfe, N., et al. 2016, ArXiv e-prints [arXiv:1612.05560]
Croxall, K. V., Smith, J. D., Pellegrini, E., et al. 2017, ApJ, 845, 96
Cutri, R. M., Wright, E. L., Conrow, T., et al. 2011, Explanatory Supplement to the WISE Preliminary Data Release Products, Tech. rep.
Decarli, R., Walter, F., Venemans, B. P., et al. 2018, ApJ, 854, 97
Díaz-Santos, T., Armus, L., Charmandaris, V., et al. 2013, ApJ, 774, 68
Fruchter, A., & Hook, R. N. 1997, in Applications of Digital Image Processing XX, ed. A. G. Tescher, Proc. SPIE, 3164, 120
Guillard, P., Boulanger, F., Lehnert, M. D., et al. 2015, A&A, 574, A32
Gullberg, B., De Breuck, C., Vieira, J. D., et al. 2015, MNRAS, 449, 2883
Helou, G., Malhotra, S., Hollenbach, D. J., Dale, D. A., & Contursi, A. 2001, ApJ, 548, L73
Herrera-Camus, R., Bolatto, A. D., Wolfire, M. G., et al. 2015, ApJ, 800, 1
Herrera-Camus, R., Sturm, E., Graciá-Carpio, J., et al. 2018a, ApJ, 861, 94
Herrera-Camus, R., Sturm, E., Graciá-Carpio, J., et al. 2018b, ApJ, 861, 95
Hirashita, H., Buat, V., & Inoue, A. K. 2003, A&A, 410, 83
Husemann, B., Wisotzki, L., Sánchez, S. F., & Jahnke, K. 2013, A&A, 549, A43
Husemann, B., Jahnke, K., Sánchez, S. F., et al. 2014, MNRAS, 443, 755
Husemann, B., Bennert, V. N., Scharwächter, J., Woo, J.-H., & Choudhury, O. S. 2016, MNRAS, 455, 1905
Husemann, B., Tremblay, G., Davis, T., et al. 2017, The Messenger, 169, 42
Husemann, B., Scharwächter, J., Davis, T. A., et al. 2019, A&A, in press, DOI: 10.1051/0004-6361/201935283
Jarrett, T. H., Chester, T., Cutri, R., et al. 2000, AJ, 119, 2498
Kauffmann, G., Heckman, T. M., Tremonti, C., et al. 2003, MNRAS, 346, 1055
Kewley, L. J., Dopita, M. A., Sutherland, R. S., Heisler, C. A., & Trevena, J. 2001, ApJ, 556, 121
Klein, R., Beckmann, S., Bryant, A., et al. 2014, in Ground-based and Airborne Instrumentation for Astronomy V, Proc. SPIE, 9147, 91472X
Langer, W. D., & Pineda, J. L. 2015, A&A, 580, A5
Lesaffre, P., Pineau des Forêts, G., Godard, B., et al. 2013, A&A, 550, A106
Luhman, M. L., Satyapal, S., Fischer, J., et al. 2003, ApJ, 594, 758
Maiolino, R., Caselli, P., Nagao, T., et al. 2009, A&A, 500, L1
Malhotra, S., Kaufman, M. J., Hollenbach, D., et al. 2001, ApJ, 561, 766
Murphy, E. J., Condon, J. J., Schinnerer, E., et al. 2011, ApJ, 737, 67
Nesvadba, N. P. H., Boulanger, F., Salomé, P., et al. 2010, A&A, 521, A65
Ogle, P., Antonucci, R., Appleton, P. N., & Whysong, D. 2007, ApJ, 668, 699
Peterson, B. W., Appleton, P. N., Bitsakis, T., et al. 2018, ApJ, 855, 141
Schulz, B., Marton, G., Valtchanov, I., et al. 2017, ArXiv e-print [arXiv:1706.00448]
Smith, J. D. T., Croxall, K., Draine, B., et al. 2017, ApJ, 834, 5
Stacey, G. J., Geis, N., Genzel, R., et al. 1991, ApJ, 373, 423
Stacey, G. J., Hailey-Dunsheath, S., Ferkinhoff, C., et al. 2010, ApJ, 724, 957
Temi, P., Marcum, P. M., Young, E., et al. 2014, ApJS, 212, 24
Wagg, J., Carilli, C. L., Wilner, D. J., et al. 2010, A&A, 519, L1
Weaver, J., Husemann, B., Kuntschner, H., et al. 2018, A&A, 614, A32
Weilbacher, P. M., Streicher, O., Urrutia, T., et al. 2012, SPIE Conf. Ser., 8451, 84510B
Weilbacher, P. M., Streicher, O., Urrutia, T., et al. 2014, in Astronomical Data Analysis Software and Systems XXIII, ASPCS, 485, 451
Yamamura, I., Makiuti, S., Ikeda, N., et al. 2009, in AKARI, a Light to Illuminate the Misty Universe, ASPCS, 418, 3

Appendix A: FIFI-LS time window selection

Although SOFIA reduces the water vapor absorption to 99% of the ground level, the atmospheric variations still play a perceptible role and affect the quality of the FIFI-LS data. To probe this effect, we used the science-ready LEVEL_3 pipeline output files. Each file corresponds to only ∼30 s of exposure time and cannot be examined independently due to the high levels of noise. Calculating [C II] line flux signal-to-noise ratio (S/N) of cumulatively summed files allows us to trace the trends of the S/N and therefore judge the atmospheric conditions. Ideally, the trend should rise as the square root function. If the S/N remains the same or even decreases when exposure time is added, we assume that an atmospheric variation degrades the quality and exclude those time windows from the analysis, as shown with the shaded areas in Fig. A.1.

To calculate the S/N as a function of the exposure time, we fit a fixed Gaussian shape taken from the fitting result before the additional selection to the spectra, summed within the 36″ diameter aperture. In the case of HE 1353−1917, when the line shape is not Gaussian, the procedure still works similarly because only relative trends are important in this analysis. Masking the spectral regions with strong atmospheric absorption lines is, conversely, very important for the flux estimations. The first few values of the S/N as a function of the coadded files are unreliable, but the overall trends remained when we performed the reverse-order coadding test.

The rapid altitude shifts also affect the S/N trends as seen in the case of HE 1353−1917 and HE 2211−3903. In the last 15 files for HE 2211−3903 the altitude is higher and of much better quality, but we decided not to exclude the majority of the files from the analysis and kept all of them.

Even though the selection due to atmospheric conditions is performed in the reduction pipeline, our additional selection technique helps to increase S/N of the detection by excluding the poor quality artifact-rich files.

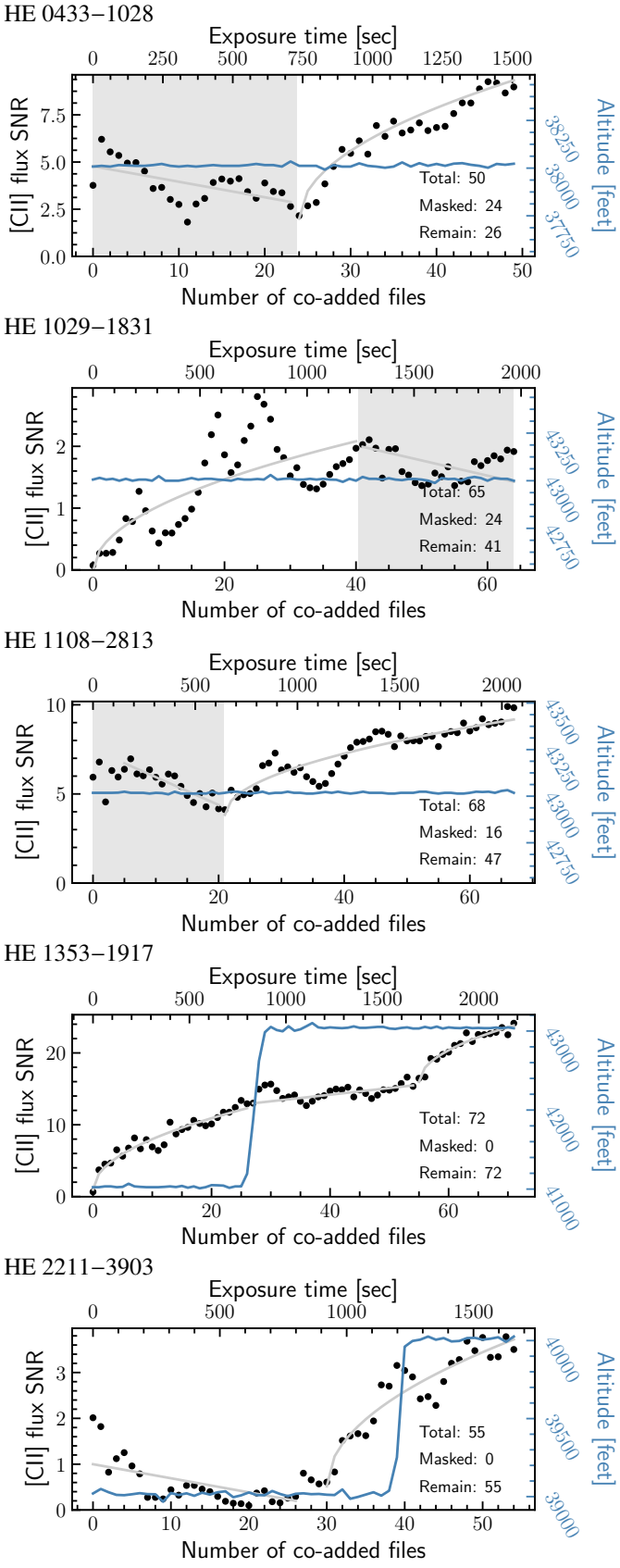

Fig. A.1. [C II] line S/N as a function of the cumulatively coadded exposures (black circles). The trends (gray lines) are purely subjective and are shown to guide the eye. The shaded areas cover the time windows and associated files that were excluded from the further analysis. The corresponding altitudes of SOFIA are shown as blue lines.

Appendix B: SED fitting

As described in Sect. 2.3, we used AGNfitter to analyze the observed galaxies. The SED plots are presented in Fig. B.1–B.5.

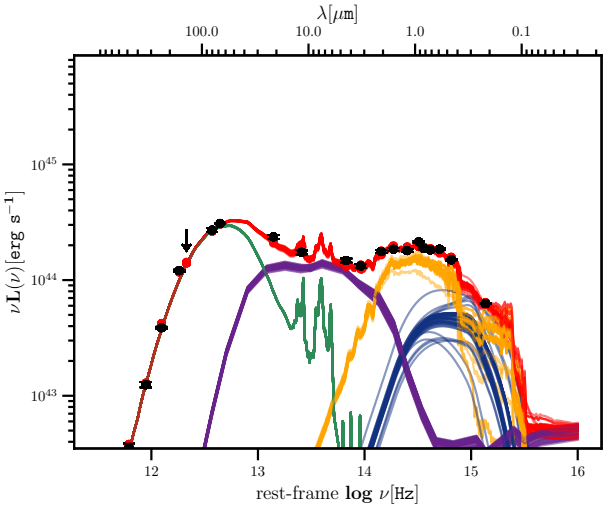

Fig. B.1. Reconstructed SED for HE 0433−1028 and best-fit SED model determined by AGNfitter (Calistro Rivera et al. 2016). We show 50 MCMC realizations fit to the broadband photometric data (black points with error bars). The red lines represent the total model, which consists of four components: the cold and warm dust in star-forming regions (green lines), the torus of AGN-heated dust (purple lines), the stellar continuum (yellow lines), and the AGN accretion disk (blue lines).

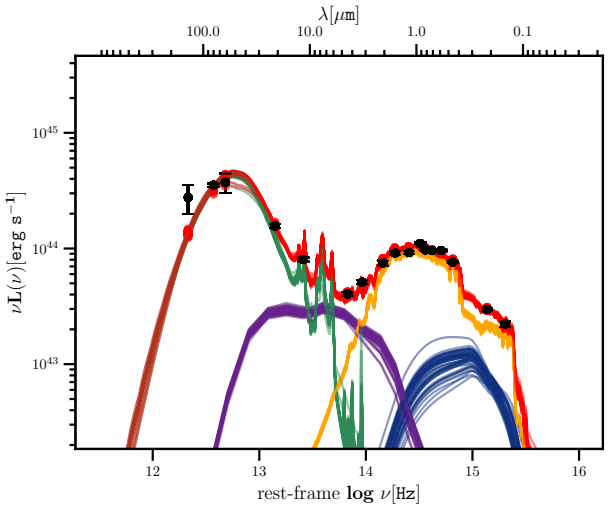

Fig. B.2. Same as Fig. B.1 for HE 1029−1831.

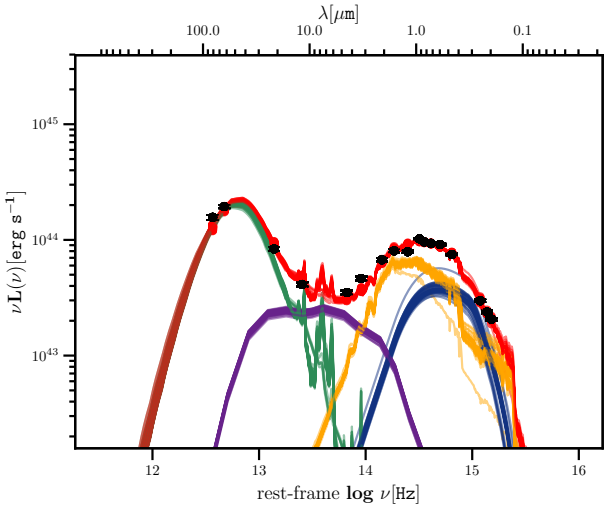

Fig. B.3. Same as Fig. B.1 for HE 1108−2813.

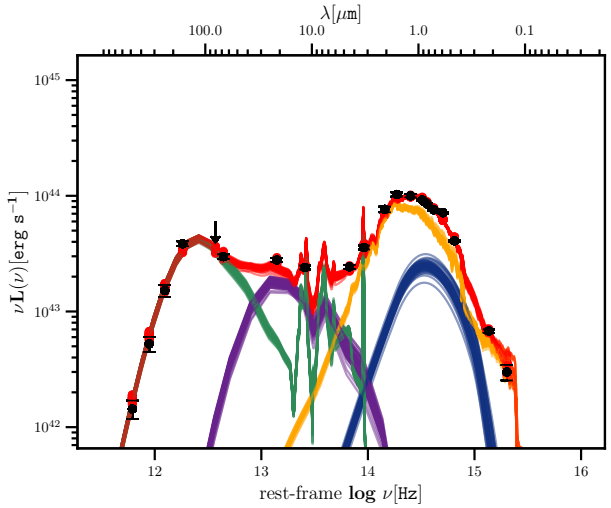

Fig. B.4. Same as Fig. B.1 for HE 1353−1917.

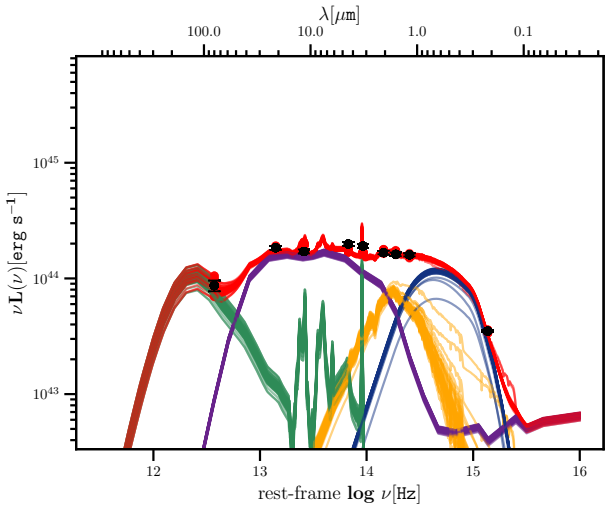

Fig. B.5. Same as Fig. B.1 for HE 2211−3903.